Materialia 15 (2021) 100967

Contents lists available at ScienceDirect

Materialia

journal homepage: www.elsevier.com/locate/mtla

Solid-state additive manufacturing of aluminum and copper using additive friction stir deposition: Process-microstructure linkages

R. Joey Griffiths[a], David Garcia[a], Jie Song[b], Vijay K. Vasudevan[b], Matthew A. Steiner[b], Wenjun Cai[a], Hang Z. Yu[a,*]

[a] Department of Materials Science and Engineering, Virginia Tech, Blacksburg, VA 24061, USA
[b] Department of Mechanical and Materials Engineering, University of Cincinnati, Cincinnati, OH 45221, USA

ARTICLE INFO

Keywords:
Solid-state additive manufacturing
Microstructure evolution
Geometric dynamic recrystallization
Discontinuous recrystallization
Texture
Misorientation

ABSTRACT

Among metal additive manufacturing technologies, additive friction stir deposition stands out for its ability to create freeform and fully-dense structures without melting and solidification. Here, we employ a comparative approach to investigate the process-microstructure linkages in additive friction stir deposition, utilizing two materials with distinct thermomechanical behavior—an Al-Mg-Si alloy and Cu—both of which are challenging to print using beam-based additive processes. The deposited Al-Mg-Si is shown to exhibit a relatively homogeneous microstructure with extensive subgrain formation and a strong shear texture, whereas the deposited Cu is characterized by a wide distribution of grain sizes and a weaker shear texture. We show evidence that the microstructure in Al-Mg-Si primarily evolves by continuous dynamic recrystallization, including geometric dynamic recrystallization and progressive lattice rotation, while the heterogeneous microstructure of Cu results from discontinuous recrystallization during both deposition and cooling. In Al-Mg-Si, the continuous recrystallization progresses with an increase of the applied strain, which correlates with the ratio between the tool rotation rate Ω and travel velocity V. Conversely, the microstructure evolution in Cu is found to be less dependent on Ω, instead varying more with changes to V. This difference originates from the absence of Cu rotation in the deposition zone, which reduces the influence of tool rotation on strain development. We attribute the distinct process-microstructure linkages and the underlying mechanisms between Al-Mg-Si and Cu to their differences in intrinsic thermomechanical properties and interactions with the tool head.

1. Introduction

The last decade has witnessed the emergence of several solid-state metal additive manufacturing technologies [1], including cold spray [2], ultrasonic additive manufacturing [3], friction stir additive manufacturing [4], and additive friction stir deposition (AFSD) [5]. Among these processes, AFSD stands out as a *freeform near-net-shaping* process that renders wrought-like microstructures and mechanical properties in the as-printed state. As the diagram shows in Fig. 1(a), the operational principle of AFSD is analogous to fused deposition modeling of polymers [6,7]. However, there are major differences: (i) friction stir is leveraged to thermally soften and deform the feed material and enable deposition [5,8–10]; (ii) beneath the rotating tool head, the material is subjected to shear deformation; and (iii) this deformation causes mixing and bonding with the substrate rather than co-melting and solidification. The process variables in AFSD affect the thermomechanical processing conditions that determine the deformation and annealing phenomena, and, in turn, control the microstructure evolution. Because AFSD allows for site-specific buildup of materials, this unlocks the opportunity for mesoscale design [11,12] via local adjustment of process variables along the printing path.

The microstructure evolution in AFSD occurs in three main stages: preheating before the material exits the tool head, deformation during deposition, and thermal exposure during cooling. In the first stage, i.e., when the feed material is inside the tool head, its temperature rises due to heat conduction from the material-substrate interface. In the second stage, i.e., during deposition, the material is under both compression and shear at elevated temperatures, with the typical peak temperatures being ~0.5–0.9 of the melting temperature of the material [9,13]. While its strain and strain rate values have not yet been measured, literature on other friction stir processes suggests high strains ranging from 5–10 and strain rates of ~5 s^{-1} or greater [14,15]. The temperature and strain rate in AFSD fall in a regime comparable to hot working, whereas the expected strain level places AFSD more akin to severe plastic deformation (SPD). Hot working conditions typically cause dynamic recrystallization to dominate, whereas SPD processes are often characterized by

* Corresponding author.
E-mail address: hangyu@vt.edu (H.Z. Yu).

https://doi.org/10.1016/j.mtla.2020.100967
Received 5 August 2020; Accepted 19 November 2020
Available online 21 November 2020

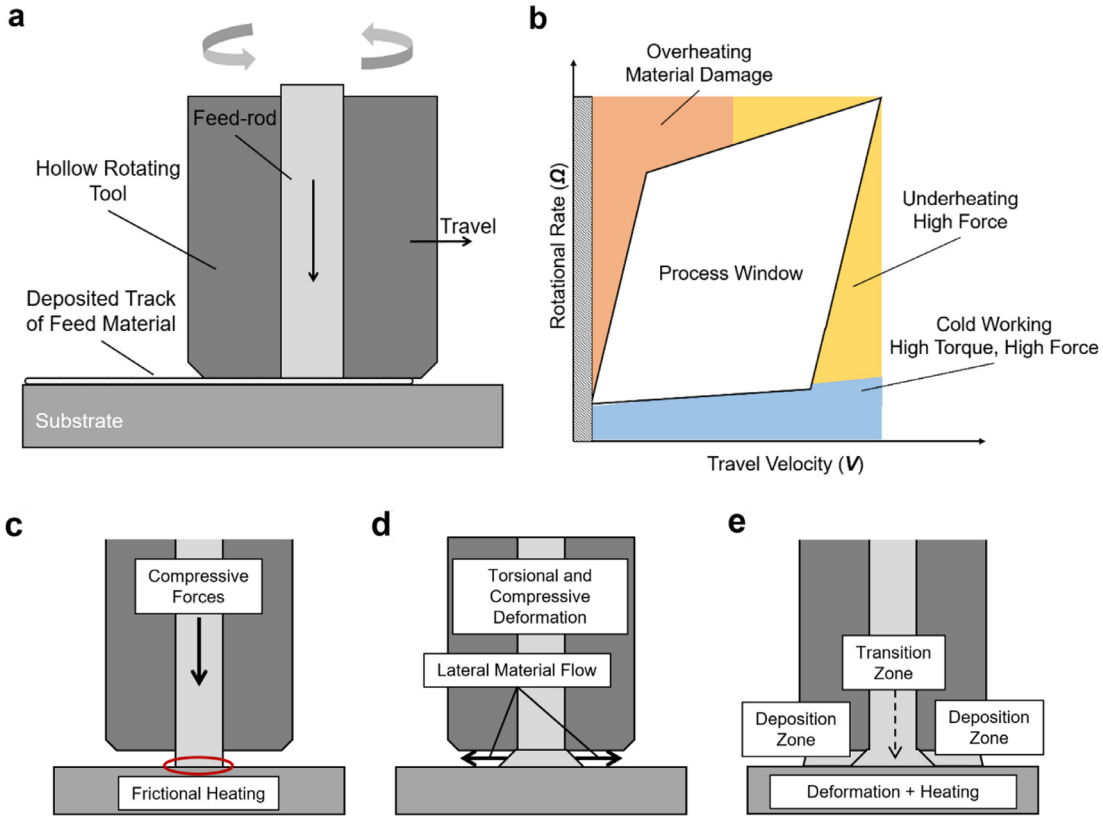

Fig. 1. AFSD process illustration. (a) Diagram of the AFSD process showing the general position and motion of the tool head and feed-rod. (b) Feasible process window defined by Ω and V. (c)–(e) Illustration of the major deformation steps during deposition, including compression and shear in the transition zone and deposition zone.

grain subdivision followed by strain-induced high angle grain boundary formation. Therefore, dynamic microstructure evolution mechanisms related to both categories may operate in the deformation stage of AFSD. In the third stage, the material experiences a deformation-free period at elevated temperatures as conduction and convection cool the material, allowing static or post-dynamic restoration phenomena to occur [16,17].

The kinetics of microstructure evolution critically depends on the AFSD process variables, which include the tool head rotation rate Ω, in-plane traveling velocity V, and material feed rate F. The rotation rate Ω generally controls the heat generation rate and strain rate, while V determines the length of time available for material deformation. As a result, the ratio Ω/V is a measure of the tool-material interaction and total strain development. F determines the amount of the deposited material per time. The process variable settings that produce fully-dense, high-quality depositions define the feasible process window in Fig. 1(b). Outside the feasible process window, e.g., at very large Ω, intense heating can cause damage to the tool head, jamming of the feed material inside the hollow channel, or melting under extreme cases. For low Ω or high F, the heat generation becomes insufficient to soften the material, preventing adequate plastic deformation for deposition. Low F and high V may lead to poor surface quality and pore formation as insufficient material is supplied for deposition.

The goal of this work is to explore the linkages between the AFSD process variables and the microstructure evolution within the feasible process window. Such linkages will allow us to tailor the microstructure for given applications through process design. For example, by controlling Ω, V, and F, AFSD may result in microstructures with ultrafine grains for grain boundary strengthening [18] or microstructures consisting of special grain boundaries for prevention of fatigue failure [19] or hydrogen embrittlement [20]. While the microstructure evolution in FSW has been extensively studied [21–23], the present study is necessary and timely given the prominent fundamental differences in mechanical constraint and thermomechanical history between AFSD and FSW. As shown in Fig. 1(c)–(e), the deposited material undergoes multiple deformation steps in AFSD, including the initial uniaxial compression that extrudes the feed material below the tool head, compression and shear in the transition zone (below the rotating feed-rod), and the final shear-dominated deformation in the deposition zone (beneath the rotating tool head) [9]. To compare, the material in FSW is only characterized by the shear-dominated deformation without an apparent macroscopic shape change. Another salient difference between AFSD and FSW is that AFSD leads to relatively uniform deformation and minor microstructural variability through thickness or width [24–27], whereas FSW features steep strain gradients and substantial microstructural differences among the stir zone, thermomechanically-affected zone, and heat-affected zone [13].

Here, we employ a comparative approach and investigate the process-microstructure linkages of two materials, an Al-Mg-Si alloy and Cu, which are challenging to print using beam-based technologies [28,29] but are readily printed with full density using AFSD [9,30]. Al-Mg-Si and Cu are characterized by distinct thermomechanical properties. The stacking fault energies (SFE) dictate the way that dislocations are resolved during and after deformation. The SFE of Al-Mg-Si is high (SFE >160 mJ/m^2 [31]); the lack of stacking faults promotes dislocation cross-slip, engaging secondary slip systems. This increases the effectiveness of recovery in resolving dislocations. The SFE of Cu is lower (SFE ~ 78 mJ/m^2 [32,33]); it thus more readily forms stacking faults due to dislocation disassociation [34]. This hinders dislocation cross-slip, requiring additional deformation mechanisms such as twinning to accommodate large deformation. The differences between Al-Mg-Si and Cu in both their shear moduli, 24 GPa versus 45 GPa [35], and Young's

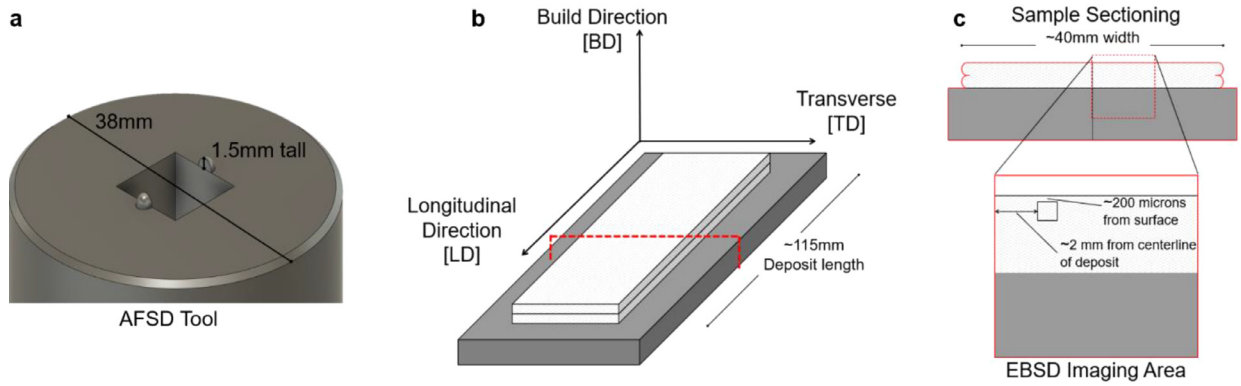

Fig. 2. Experimental details. (a) A diagram showing the bottom surface of the tool head with protrusion details. (b) A diagram of the typical configuration of the deposits with the sample axes labeled. (c) Specific sample sectioning and EBSD image location.

moduli, 70 GPa versus 117 GPa [36], will affect the deformation during AFSD. The higher overall stiffness of Cu may reduce the readiness at which the feed material plasticizes and spreads, as well as how the deposit behaves beneath the tool head. Given these salient differences, a comparative study of Al-Mg-Si and Cu will allow us to explore new physical insights into the role of intrinsic material properties in microstructure evolution in AFSD.

2. Experimental procedures

2.1. Materials and deposition

The materials used in this experiment, an Al-Mg-Si alloy and Cu, were purchased as AA 6061 and Cu 110 (McMaster Carr, Atlanta GA, USA), respectively. These materials were used as the feed-rod and substrate, with the feed material having a 9.525 × 9.525 mm cross section and the substrate being a 6.25-mm-thick plate. For both the feed-rod and plate, Al-Mg-Si was supplied in the AA 6061-T6 heat treated condition, and Cu was supplied in the H02 or "half-hard" tempered condition.

AFSD was carried out using a MELD R2 system (MELD Manufacturing Corporation, Christiansburg VA, USA). The bottom surface of the tool head was flat except for two small protrusions adjacent to the feed rod channel. As illustrated in Fig. 2(a), the protrusions were 1.5 mm tall with rounded surfaces, and their curved shape was designed to promote material flow around them [8]. The substrate and a steel backing plate were clamped onto the print bed, and the sides of the feed-rod were coated with graphite lubricant before loading into the hollow channel of the tool head. Initially, the tool head and the loaded feed-rod were spun up to the target rotation rate Ω above the substrate. Afterwards, the tool head was lowered until its distance to the substrate reached the target layer thickness (0.765 mm for this work) and the tool protrusions partially plunged into the substrate surface. The actuator then pushed the feed material out of the tool channel until it contacted the substrate surface while rotating. The frictional heating and compressive loading from the actuator allowed the feed material to yield and spread between the space between the tool head and substrate.

Upon material yielding, a G-code script was run for controlled and consistent motion of the tool head and deposit. The used pattern was a 75 mm-long travel along the longitudinal direction, followed by a 0.765 mm lift of the tool along the build direction, followed by a 75 mm-long travel back along the longitudinal direction. This pattern resulted in a total of two layers (115 mm long) of material for each processing condition. The ratio of feed rate F to tool travel velocity V was kept at 1:3 for all depositions in this work. Table 1 summarizes the different process variables used for each sample in this study. For each material system, the lowest Ω condition was selected based on the rounded minimum Ω that enabled successful deposition.

Table 1
Summary of the processing conditions for depositing Al-Mg-Si and Cu in this work. For the sample notation, 'Low' means that the tool rotation rate and travel velocity are both low. 'High' means that the tool rotation rate and travel velocity are both high. 'Mixed' means that the tool rotation rate is high but the travel velocity is low.

Sample	Rotational Rate Ω (RPM)	Travel Velocity V (mm/s)
Al-Low	200	1
Al-Mixed	600	1
Al-High	600	3
Cu-Low	300	1
Cu-Mixed	600	1
Cu-High	600	3

2.2. Characterization methods

During material deposition, the material flow was monitored from the leading edge using an AM4115ZT digital microscope (Dino-Lite, Torrance, CA, USA). The details of the monitoring set-up have been elaborated by Garcia et al. [9]. Microhardness testing was performed using an LM310 Microvickers indenter (Leco, St. Joseph, MI, USA) using a 10 N load and an indenter dwell time of 15 s. The indents were made on the transverse cross-section across the width of the first and second layers, approximately centered through the height of each layer.

For microstructure characterization, each sample was first cross-sectioned halfway through the length of the sample (dotted outline in Fig. 2(b)), then further reduced for mounting and polishing. Sections were mounted on a conductive polymer puck and electropolished using a mixture of sulfuric acid and methanol for Al-Mg-Si, and a mixture of phosphoric acid, ethanol, and water for Cu. The imaging region was the same for all samples, located slightly off from the centerline of the deposit and roughly 200 μm below the surface of the deposit, as illustrated in Fig. 2(c). Cross sections of the feed material (denoted as Al-Base and Cu-Base) were prepared and characterized using similar approaches, but imaged in the center of the cross section.

Microstructural characterization was carried out using a Helios Nanolab 600 DualBeam SEM (FEI company, Waltham, MA, USA) equipped with an integrated energy-dispersive X-ray spectroscopy (EDS), electron backscatter diffraction (EBSD) system, and a Hikari EBSD detector. EBSD scan data analysis and alignment were performed using TSL OIM Analysis. The images generated from the scan data included inverse pole figure (IPF) maps, pole figures (PFs), orientation distribution functions (ODFs), and kernel average misorientation (KAM) maps. For the IPF maps, PFs, and ODFs shown in this work, the scan data has been rotated to align with a specific texture component described

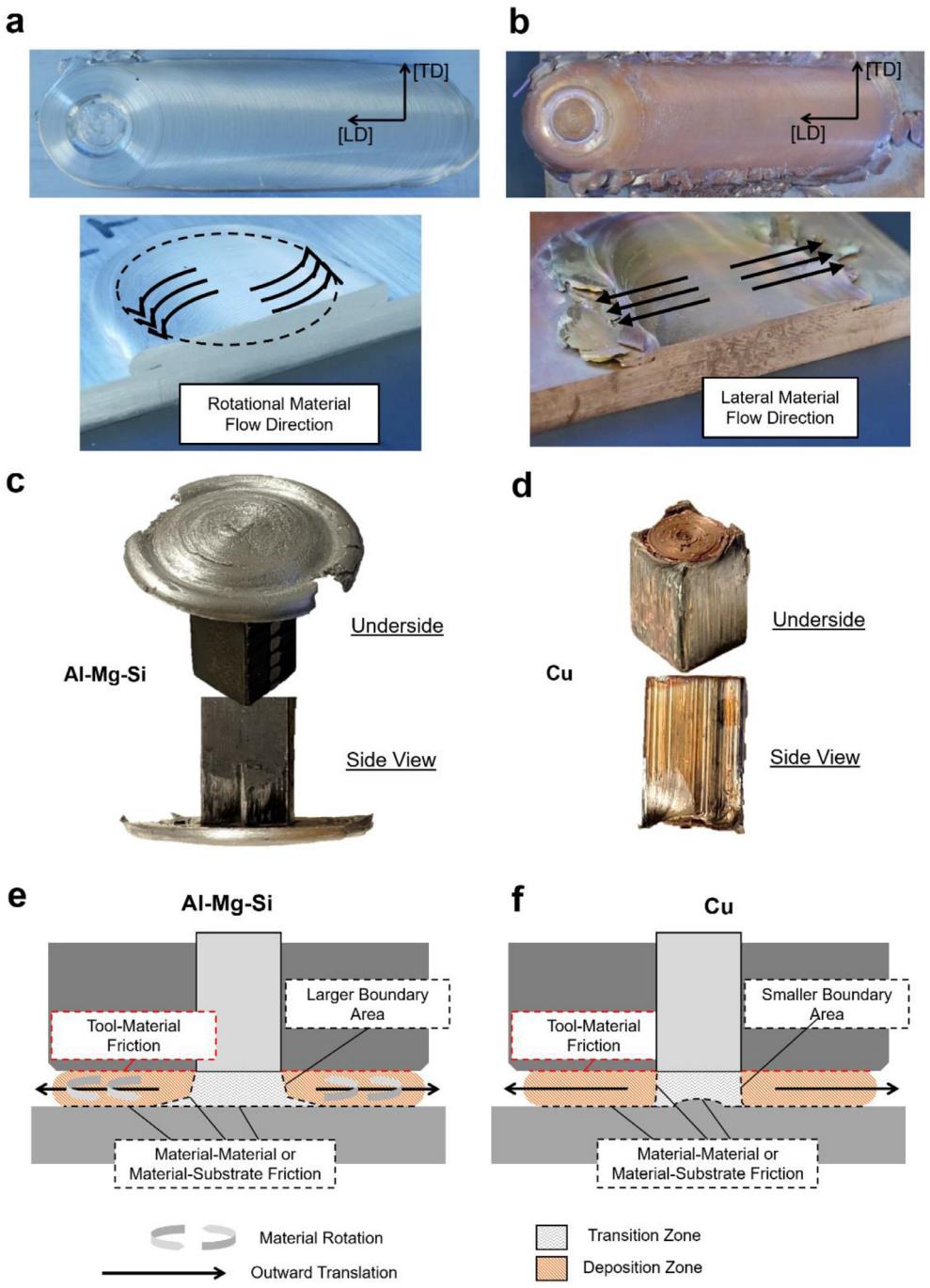

Fig. 3. A comparison of the deformation flow during AFSD of Al-Mg-Si and Cu. Top-down and cross-sectional views of (a) Al-Mg-Si and (b) Cu deposition tracks. The images of the end of feed-rod showing deformation and spreading in (c) Al-Mg-Si and an inverted cusp shape in (d) Cu. Illustration of the material rotation and feed-rod deformation for (e) Al-Mg-Si and (f) Cu.

in Section 3.4. PFs were generated with a resolution of 5° and inversion symmetry. ODFs were produced with a resolution of 0.1°. Finally, the KAM maps were generated with a misorientation range of 0 to 5° using first nearest neighbors.

In addition to the microstructure of a given area in the cross-section, the macrostructure of the whole cross-section may offer information about the material flow and deformation states, as seen in friction stir welding [13]. However, the microstructure resulting from AFSD is relatively uniform because all the deposited material undergoes severe plastic deformation at elevated temperatures. As a result, the material flow features are largely absent from cross-sectional imaging of the macrostructure. This point has been confirmed by an on-going work by the authors, so macrostructure characterization of the cross-section is not included in this work.

3. Results

3.1. Material deformation and flow behavior during AFSD

From the digital microscope, drastically different types of material deformation and flow behavior are observed during AFSD of the two materials. In Al-Mg-Si, substantial rotational motion is observed in the deposition zone, and excess feed material exits the deposition region in the form of rounded flash (shown in Fig. 3(a)). Contrary to this, almost no rotational motion is observed in the deposition zone of Cu, wherein the deposited material is pushed laterally due to the input of new material. As a result, the flash exits the deposition area along the transverse direction in the form of flat sheets (shown in Fig. 3(b)). As rotational material flow generates additional shear forces in the bulk of the depo-

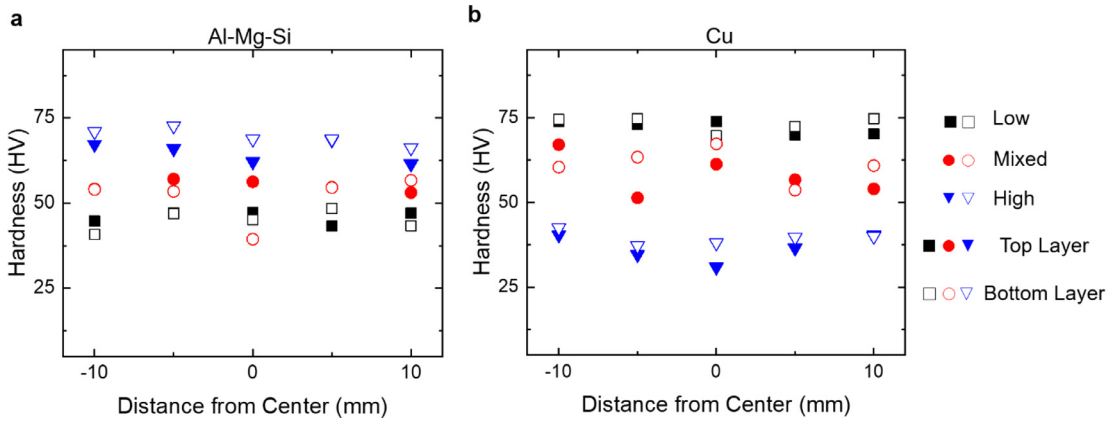

Fig. 4. Microhardness testing results for the deposited (a) Al-Mg-Si and (b) Cu, with indentations across the width of the top and bottom layers. Data points are collected for various processing conditions listed in Table 1: low rotation rate and low travel velocity (Low), high rotation rate and low travel velocity (Mixed), and high rotation rate and high travel velocity (High).

sition zone, Al-Mg-Si is more severely deformed than Cu, which mainly experiences frictional forces at the tool-material interface.

These observations also suggest that the sticking coefficient at the tool-material interface is higher in Al-Mg-Si than that of Cu, which is close to zero. The sticking coefficient is expected to vary locally, decreasing with increased surface contact velocity [37,38]. The sticking coefficient is tied to the material properties, notably the friction coefficient between the tool and deposited material. For material sticking to occur, a higher friction coefficient is required for providing sufficient shear stress to drive the material flow with the rotating tool head. In general, the reported friction coefficients of Al-steel (i.e., deposit-tool) are higher than those of Cu-steel [39], and here we observe better sticking in the deposition of Al-Mg-Si than Cu.

The state of the feed material after deposition provides insight into the deformation in the transition zone (i.e., beneath the rotating feed-rod). Fig. 3(c) and (d) shows the ends of the feed-rods after they are lifted from the deposition track. The Al-Mg-Si feed-rod is characterized by a wide, flared-out, bowl shape. In contrast, the Cu feed-rod keeps its original square shape until it finally bulges out from compressive loading, resulting in a concave cusp at the end. This observation suggests a much larger boundary area between the transition zone and deposition zone and larger deformation in the transition zone in Al-Mg-Si compared to Cu.

Based on the material flow observation and the feed-rod geometry after deposition, Fig. 3(e) and (f) illustrates the differences of Al-Mg-Si and Cu in the material rotation and the transition zone profile. The findings in Fig. 3 suggest that Al-Mg-Si undergoes considerably larger total deformation than Cu through the whole AFSD process, both in the transition and deposition zones.

3.2. Microhardness

Fig. 4 plots the measured Vickers Hardness (HV) of the deposited Al-Mg-Si and Cu. The goal of this test is to examine the uniformity of the mechanical properties after AFSD. For Al-Mg-Si, we find a hardness standard deviation of ±1.47 HV between the top and bottom layers of the deposits, and ±2.82 HV across the width of the samples. For Cu, these values are ±1.17 HV and ±3.20 HV, respectively. The small standard deviations of hardness suggest a rather uniform microstructure across the deposits, which is consistent with previous AFSD studies [24]. Noting this minimal variation, the average hardness values for Al-Low, Al-Mixed, and Al-High are 45.4, 53.3, and 67.3 HV, respectively. For Cu-Low, Cu-Mixed, and Cu-High, these values are 72.7, 59.6, and 38 HV respectively.

Under all processing conditions, the hardness values of the as-deposited Al-Mg-Si and Cu are significantly reduced from the hardness values of feed materials, which are 110 HV and 112 HV, respectively. For the Al-Mg-Si feed-rod, hardening occurs predominately through precipitates that are sensitive to the thermomechanical conditions. Thus, the significant softening is expected to stem from the dissolution, growth, or deterioration of the optimal precipitate structure achieved through the T6 heat treatment [40]. The Cu feed-rod is hardened via cold-working and grain refinement, but the restoration mechanisms in AFSD lead to significant reduction of the dislocation density and soften the material (shown and discussed further in Sections 3 and 4). The plots in Fig. 4 also show that the hardness changes noticeably with process variables, highlighting the large processing space available with AFSD; a wide range of mechanical properties can be readily produced through process control. We note that complete identification of the comprehensive relationship among process, microstructure, and mechanical properties is beyond the scope of this work, which focuses on the process-microstructure linkage. An in-depth investigation into the microstructure-property linkage for AFSD is better suited to its own study.

3.3. Characteristic grain structures: Al-Mg-Si vs. Cu

Figs. 5 and 6 present the IPF maps and grain boundary misorientation distributions of Al-Mg-Si and Cu, respectively. Both figures include data of the feed material and the deposits from three process conditions. For the IPF maps of the deposits, the EBSD data has been rotated to better present a particular shear texture, as further described in Section 3.4. The corresponding shear direction is annotated on the bottom right of the IPF maps. The normal of the shear plane is 90° from the shear direction and approximately in plane with the IPF map image. For the grain boundary misorientation distributions, since substructure formation is expected, the minimum misorientation constituting a grain boundary has been set at 2°. Low angle boundaries (LABs) are classified as boundaries with misorientation angles in the range of 2 to 15°, and high angle boundaries (HABs) classified as boundaries with misorientation greater than 15°. Fig. 7 presents the grain size distribution for each material-process condition combination and the feed material.

The feed material Al-Base has large grains with no evident intragranular misorientation, which would appear as an orientation (color) gradient within a single grain. Cu-Base shows a finer microstructure than Al-Base, and an abundance of grains have residual local misorientations due to its cold-worked state. Both feed materials are in the form of drawn rods, but Al-Base has an additional heat treatment step (T6 condition), which effectively removes the local misorientations formed during drawing.

As shown in Figs. 5 and 7(a), the Al-Mg-Si deposits all show grain refinement from Al-Base, most evidently in Al-Low and Al-Mixed, wherein the area-weighted average grain size significantly reduces from 113 μm in the feed material to 10 and 16 μm, respectively. Given the low number of grains in the imaging area for Al-High, the grain size presented

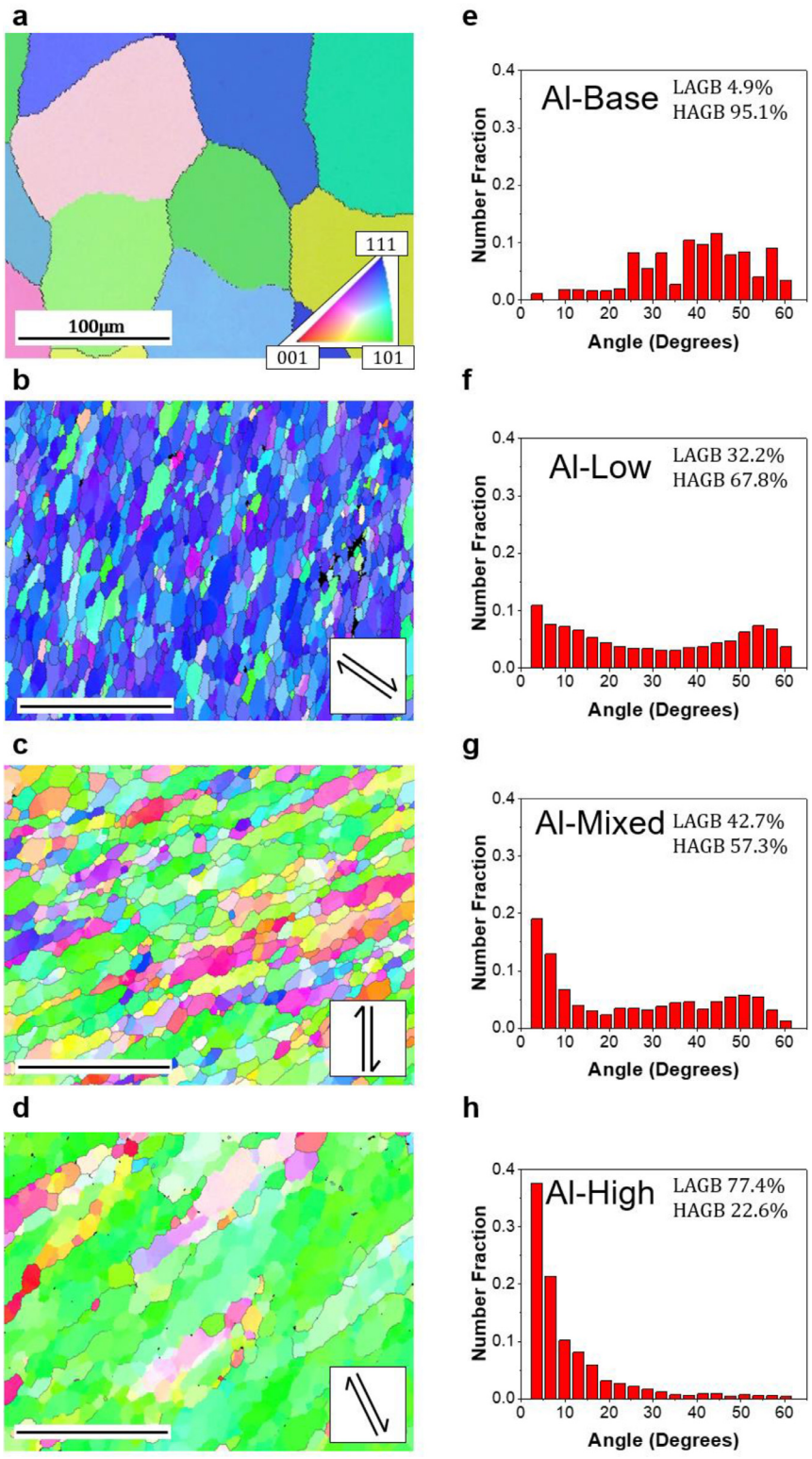

Fig. 5. Microstructure characterization of Al-Mg-Si. The IPF map and grain boundary misorientation distribution are shown for ((a) and (e)) the feed material, ((b) and (f)) Al-Low, ((c) and (g)) Al-Mixed, and ((d) and (h)) Al-High. The shear direction is labeled in the IPF map for each deposited sample.

in 7(d) is not necessarily representative of the whole sample; however, the IPF map undoubtedly shows significant deformation that the large grains are substantially flattened and elongated as compared to the feed material. All of the Al-Mg-Si deposits show substantial substructure formation. Comparing Al-Low and Al-Mixed, the former has a smaller average grain size and a lower grain size standard deviation, whereas the grains in the latter appear flattened and elongated similarly to those in Al-High—but on a much smaller length scale, approximately 1–2 subgrains thick. From the misorientation distribution, all the Al-Mg-Si deposits exhibit a considerably high fraction of LABs, with an increasing percentage of 32.2%, 42.7% and 77.4% across Al-Low, Al-Mixed, and Al-High respectively. The correlation of grain refinement and LAB fraction suggests that the restoration phenomena of Al-Mg-Si during AFSD are primarily governed by recovery and continuous dynamic recrystallization involving subgrain formation and subsequent rotation.

The recrystallization is most complete in Al-Low and least complete in Al-High. The observation of severely elongated grains and the

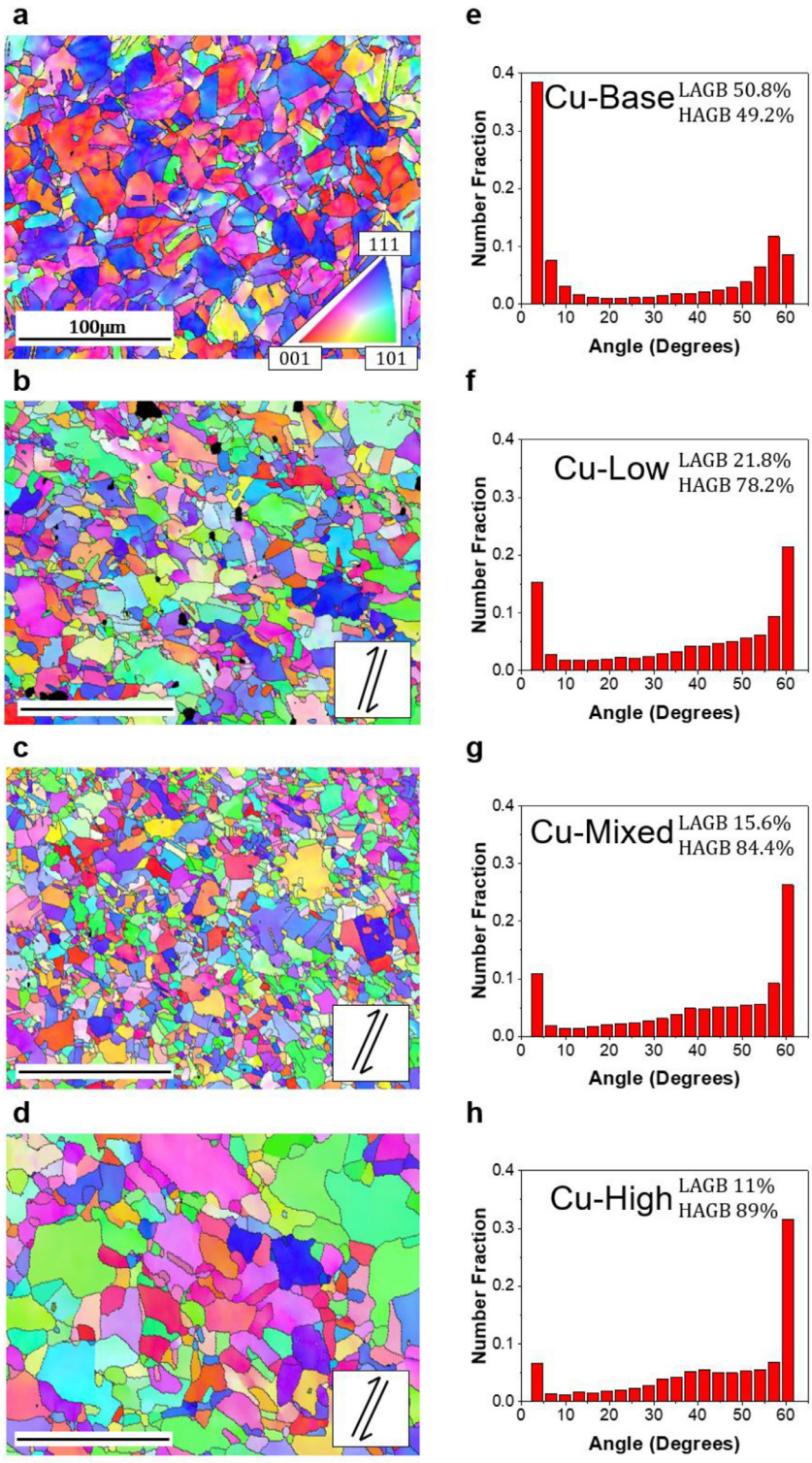

Fig. 6. Microstructure characterization of Cu. The IPF map and grain boundary misorientation distribution are shown for ((a) and (e)) the feed material, ((b) and (f)) Cu-Low, ((c) and (g)) Cu-Mixed, and ((d) and (h)) Cu-High. The shear direction is labeled in the IPF map for each deposited sample.

pinch-off phenomenon at serrated boundaries further suggests the role of geometric dynamic recrystallization [16], which will be elaborated in Section 4.1. We note that in a previous study on AFSD of Al-Mg-Si utilizing a different tool geometry and a different range of process settings, more equiaxed grain structures have been observed as a result of complete recrystallization [41]. Finally, it is interesting to note that the shear direction (labeled in each IPF map) varies among Al-Low, Al-Mixed, and Al-High, but it always appears roughly 45° from the elongation axis of the grains.

Instead of forming elongated or flattened grains during AFSD, Cu exhibits roughly equiaxed grains for all process variable settings, as seen in Fig. 6. Both Cu-Low and Cu-Mixed show grain size reduction from the feed material Cu-Base, but with a heterogeneous grain structure consisting of larger grains intermixed with smaller ones. Fig. 7(b) plots the grain size distribution, and the area-weighted average grain size of Cu-Base, Cu-Low, Cu-Mixed, and Cu-High is determined to be 18, 14, 10, and 27 μm, respectively. Comparing Cu-Low and Cu-Mixed, the latter has a lower peak grain size than the former and exhibits a

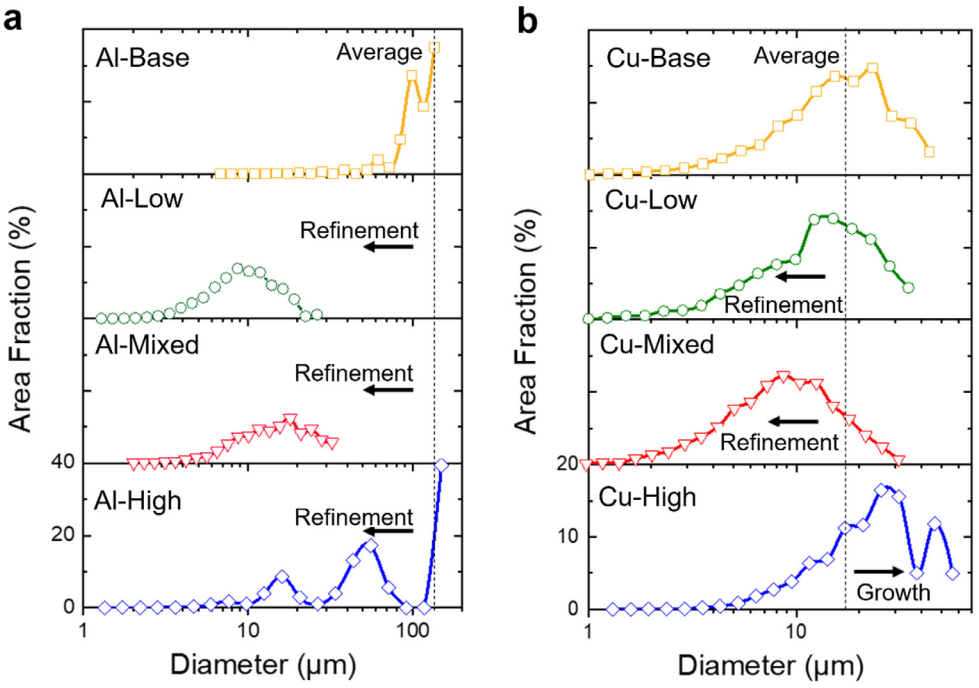

Fig. 7. Grain size distribution with a comparison of the feed-rod and the deposits for (a) Al-Mg-Si and (b) Cu.

lower fraction of LABs, 15.6% as compared to 21.8%, which is shown in Fig. 6(f) and (g). Given the heterogeneous nature of the resultant microstructure, the grain refinement in Cu-Low and Cu-Mixed is likely the culmination of multiple restoration phenomena with discontinuous recrystallization being an important mechanism, which is commonly observed in worked Cu [42,43]. Cu-High is also characterized by a wide grain size distribution but shows an increase of the average grain size as compared to the feed material. In addition, Cu-High exhibits a lower LAB fraction, 11%, than Cu-Low and Cu-Mixed, signifying more HAB migration. Despite the differences in grain size and misorientation distribution, the shear directions in all deposited Cu are nearly identical.

To continue, the local misorientation, which correlates directly to geometrically necessary dislocations (GNDs), can be characterized using KAM maps. Fig. 8 presents the KAM maps for each material-process condition combination. Only a small degree of intragranular misorientation is observed inside the grains of the Al-Mg-Si feed material. After AFSD, the KAM maps show a relatively 'ordered' spatial distribution of local misorientation, which appears prominently along LABs or subgrain boundaries that result from dislocation annihilation and rearrangement. Compared to Al-Low or Al-Mixed, the distribution of misorientations in Al-High indicates less complete restoration.

In the feed material of Cu, nearly all grains contain local misorientations, further highlighting the stored energy in Cu-Base because of its cold-worked state. After AFSD, Cu shows a decreased global content of dislocations from its original state. The spatial distribution of local misorientation in Cu is more heterogeneous than Al-Mg-Si, with certain regions containing accumulated local misorientations and others almost entirely free of them. This is particularly notable in Cu-High, which mainly consists of 'clean' grains with minimal intragranular misorientations or substructures. The characteristics of the KAM and IPF maps suggest that the microstructure of Cu largely results from discontinuous recrystallization processes that can eliminate local misorientations via HAB migration.

3.4. Texture development

Figs. 9 and 10 show the PFs and ODFs for the deposited Al-Mg-Si and Cu, all of which display evidence of certain types of shear texture.

Table 2
Ideal FCC shear textures and the corresponding crystallographic directions.

Component	{hkl}<uvw>
A_1^*	{111}<$\bar{1}1\bar{2}$>
A_2^*	{111}<$11\bar{2}$>
A	{1 $\bar{1}$ 1}<110>
$\bar{A}$	{1 $\bar{1}$ 1}<$\bar{1}\bar{1}$0>
B	{1 $\bar{1}$ 2}<110>
$\bar{B}$	{$\bar{1}$ 11}<$\bar{1}\bar{1}$0>
C	{001}<110>

The orientation of the PFs has been rotated to lock onto the C-type shear component as in the IPF maps of Figs. 5 and 6. Shear textures are commonly observed in deformation processing that involves large strains, such as friction stir welding [44], torsion-based processes [45], and wear [46]. Table 2 summarizes the ideal shear texture types for FCC metals and their coordinate systems [44,47,48].

For Al-Mg-Si, Al-Low exhibits a weak C-type shear texture and a strong B/$\bar{B}$ type; both Al-Mixed and Al-High exhibit strong C-type shear texture. It is known that the type of shear texture correlates to the applied strain values, with A-type typically forming first (the shear strain $\gamma \sim 1$), followed by B-type ($\gamma \sim 3$–6), and then C-type ($\gamma > 10$) [49]. This progression suggests that Al-Low may be associated with lower total shear strain than the others. For Cu, all three samples show similar textures consisting of B/$\bar{B}$ and C components. Cu-Low also has an A_1^* component. Since the texture observed in Cu is a convolution of the deformation and discontinuous recrystallization, it is unrealistic to compare the strain levels in these samples based on the texture results alone.

Comparing the pole figures between Al-Mg-Si and Cu, a much stronger texture is observed in the former, noting the different scales of xRandom used for the two materials. One reason for that is the larger total strain developed in Al-Mg-Si during feeding and during material flow under the rotating tool head, which has been explained in Section 3.1. Another factor is the difference in their microstructure evolution mechanisms. Al-Mg-Si undergoes a continuous type of recrystallization via subgrain formation without substantial consequences on deformation

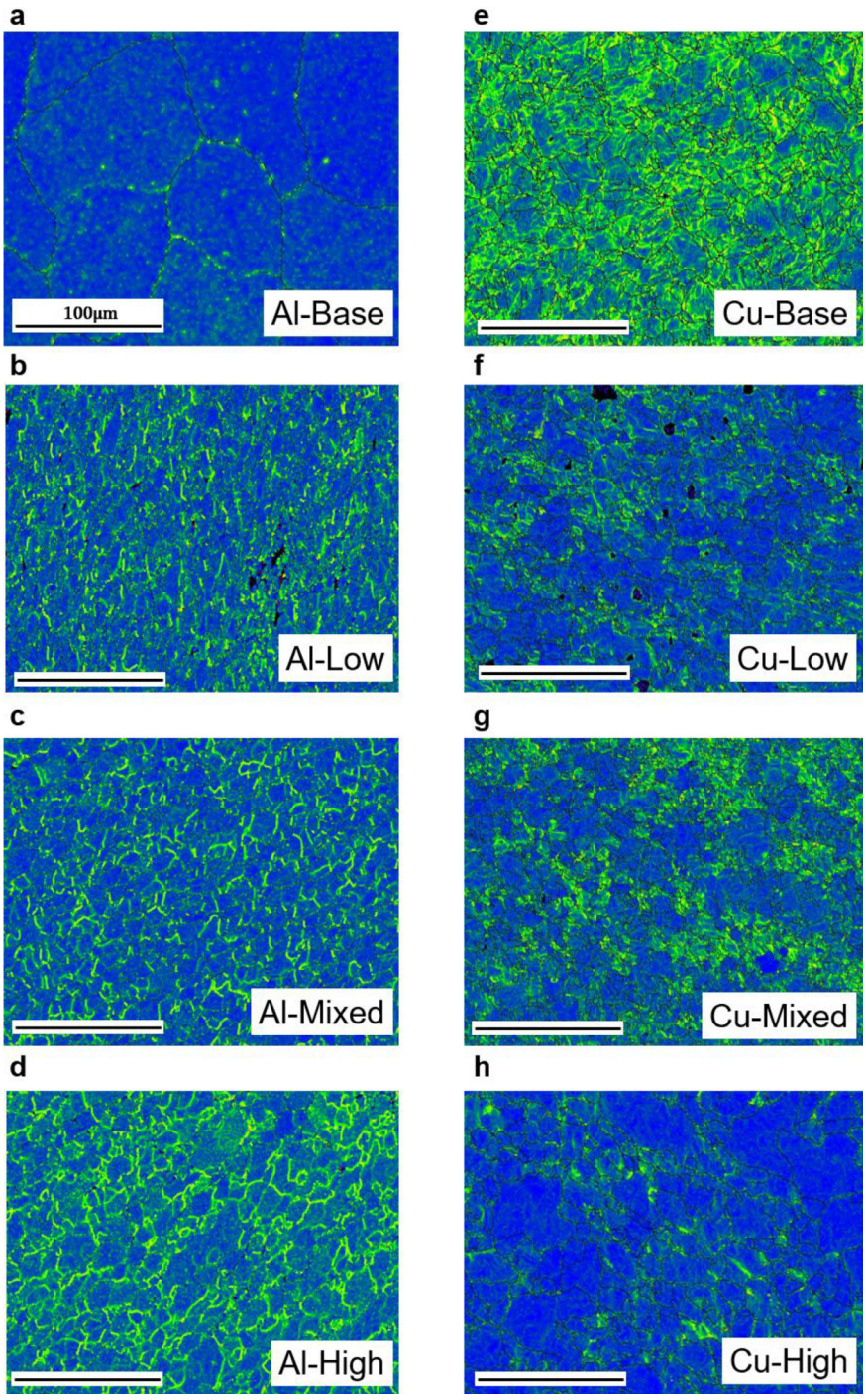

Fig. 8. A comparison of the KAM maps: (a) Al-Mg-Si feed material, (b) Al-Low, (c) Al-Mixed, (d) Al-High, (e) Cu feed material, (f) Cu-Low, (g) Cu-Mixed, and (h) Cu-High.

texture. In contrast, Cu undergoes a discontinuous type of recrystallization, which can effectively weaken the deformation-induced texture when new orientation-independent grains nucleate and grow.

4. Origin of the process-microstructure linkages in AFSD

4.1. Al-Mg-Si

4.1.1. Restoration phenomena in Al-Mg-Si: recovery and continuous dynamic recrystallization

As shown in Figs. 5 and 8, the deposited Al-Mg-Si is characterized by a comparatively homogeneous microstructure with elongated grains separated by serrated boundaries. Fig. 11(a) provides evidence that some newly recrystallized grains form as the elongated grains pinch off, characteristic of geometric dynamic recrystallization (GDRX). GDRX is typically observed in materials with high SFE, e.g. Al, during large deformation. Dynamic recovery results in gradual subgrain formation; with sufficient deformation, the initial high angle grain boundaries approach the same spacing as the subgrain size. GDRX progresses as the applied strain increases. The final fully recrystallized grain size equals the sub-grain size D, which is a function of the flow stress σ or the Zener–Hollomon parameter Z during thermomechanical processing [16]: $D = K\frac{bG}{\sigma} \propto [sinh^{-1}(\frac{Z}{A})]^{-1/n}$. Here, b is the Burgers vector; G is the shear modulus; K, n, and A are constants depending on the specific material.

Along with the dominant GDRX mechanism, there is evidence of progressive lattice rotation, which has been observed in large deformation

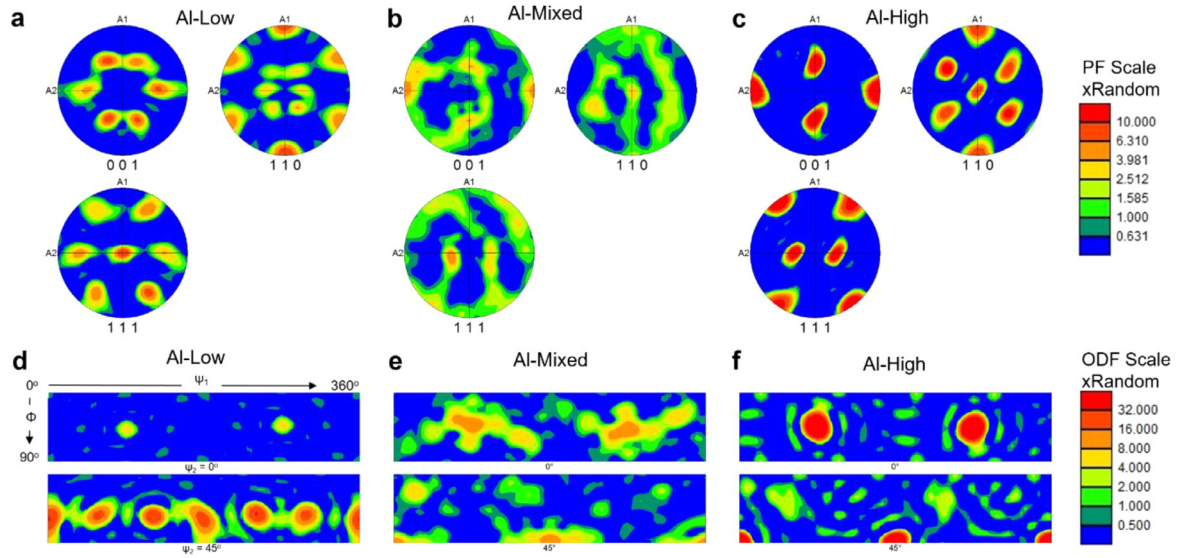

Fig. 9. Texture of the deposited Al-Mg-Si. Pole figures and orientation distribution functions are shown for ((a) and (d)) Al-Low, ((b) and (e)) Al-Mixed, and ((c) and (f)) Al-High.

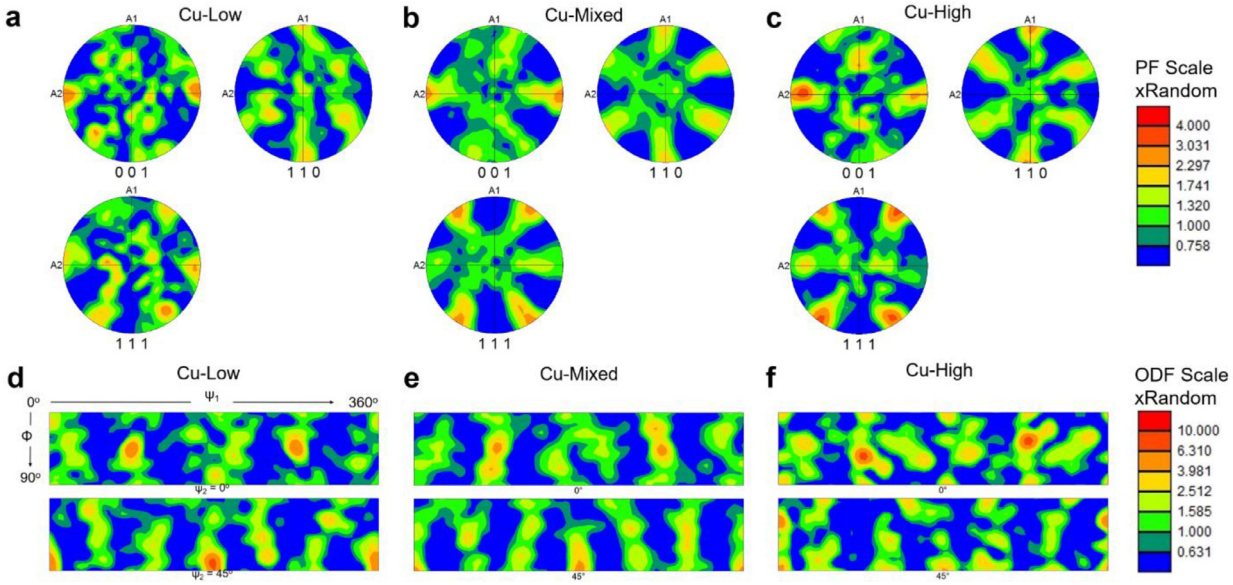

Fig. 10. Texture of the deposited Cu. Pole figures and orientation distribution functions are shown for ((a) and (d)) Cu-Low, ((b) and (e)) Cu-Mixed, and ((c) and (f)) Cu-High.

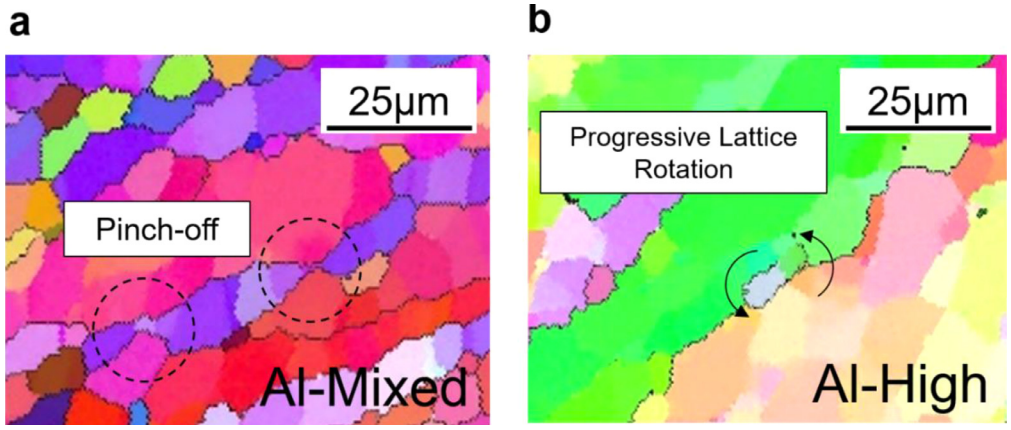

Fig. 11. Restoration mechanisms in AFSD of Al-Mg-Si. (a) Highlight of an area in Al-Mg-Si deposited at 600 RPM and 1 mm/s, which appears close to being "pinched off", forming new grains via geometric dynamic recrystallization. (b) Highlight of a surface subgrain in Al-Mg-Si deposited at 600 RPM and 3 mm/s, which is partially rotated from the parent grain, showing grain formation via progressive lattice rotation.

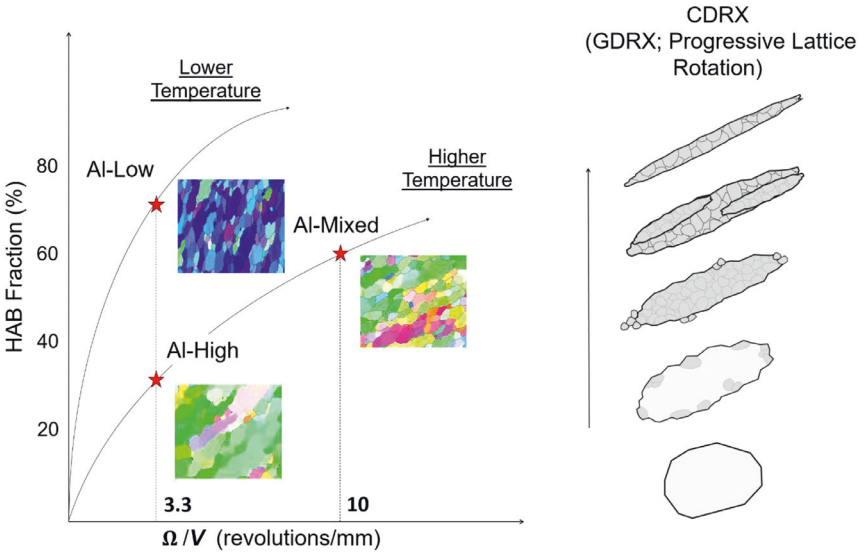

Fig. 12. Processing influences on the microstructure evolution during AFSD of Al-Mg-Si. Left: the HAB fraction, or the degree of recrystallization, is plotted against the characteristic processing parameter Ω/V. Right: illustration of the microstructure evolution process, which is characterized by CDRX, including GDRX and progressive lattice rotation.

of Al-Mg alloys from previous works [50,51]. Progressive lattice rotation normally occurs in subgrains adjacent to serrated grain boundaries, when local shear stresses cause a higher misorientation near the edge of the preexisting grain than its center. As the strain increases, sufficiently large misorientations may develop, forming new grains along the previous grain boundaries. Fig. 11(b) highlights an example found in Al-High from this work, wherein a subgrain at a serrated grain boundary appears to be partially rotated and could eventually become a new grain if the local strain is sufficient. As classified by Humphreys and coworkers [16], both GDRX and progressive lattice rotation belong to continuous dynamic recrystallization (CDRX).

4.1.2. Effects of strain and temperature on the degree of recrystallization

For GDRX, the degree of recrystallization is typically governed by the total strain [52,53]. Comparing the three Al-Mg-Si deposits from this work (recall Fig. 5), Al-High clearly displays the least degree of recrystallization; Al-Mixed is largely recrystallized but still contains a fraction of elongated grain structures; Al-Low is the most recrystallized with the largest fraction of HABs. This observation thus implies that Al-Low corresponds to a larger total strain compared to Al-Mixed and Al-High. However, this is contradictory to the texture observation in Fig. 9, which suggests a lower strain level in Al-Low than the other two.

From the processing perspective, the shear strain rate due to substantial material flow in the deposition zone depends on the rotation rate Ω, while the time of tool-material interaction in the deposition zone depends on $1/V$. Therefore, the total strain likely correlates with Ω/V in AFSD of Al-Mg-Si. This is supported by the FSW literature, which shows that the total strain in Al alloys increases with Ω/V [54]. With a lower Ω/V, Al-Low is then expected to exhibit a lower total strain level than Al-Mixed. This conclusion is consistent with the texture observation but not the recrystallization analysis from Fig. 5.

This seeming discrepancy may be resolved by considering the temperature influences on precipitate evolution. The feed material of AA 6061 is in the T6 state, in which β" phase precipitates lead to its peak strength. During AFSD, the peak temperatures of Al-Low, Al-Mixed and Al-High are ~706 K, 824 K, and 763 K, respectively [9]. For the latter two, the peak temperature is close to or above the solutionizing temperature of AA 6061 [55]. The high temperature condition combined with the severe deformation during AFSD likely results in partial or full dissolution of the β" phase, which has been widely reported in the FSW literature [56]. Al-Low corresponds to the lowest temperature condition, and the peak temperature is well below the precipitate solvus temperature. The presence of second phase particles during AFSD can increase the dislocation density; for a high SFE material like Al-Mg-Si, high-density tangled dislocations arise around the precipitates [57]. This effect promotes more rapid incidental boundary and subgrain formation via Zener pinning [16], effectively increasing the continuous recrystallization rate at a given strain level. Therefore, Al-Low is seen to exhibit more complete recrystallization than Al-Mixed despite the lower anticipated strain input.

To summarize, all the Al-Mg-Si deposits undergo CDRX during AFSD, which progresses with an increase of the strain input or Ω/V. Simultaneously, the recrystallization rate is influenced by the peak temperature of the system due to its effect on precipitate evolution. This explanation is illustrated in Fig. 12 by plotting the HAB fraction, which characterizes the degree of continuous recrystallization, against the characteristic processing parameter Ω/V.

4.2. Cu

4.2.1. Restoration phenomena in Cu: discontinuous dynamic recrystallization and post-dynamic, static recrystallization

The deposited Cu is characterized by a wide distribution of grain sizes, wherein the smaller grains ($d < d_{mean}$; $d_{mean}$is the mean grain size) appear in networks. This feature is shown in Fig. 13(a) and (b). The overall magnitude of the local misorientation in the deposited Cu (Fig. 8(f), (g), and (h)) is lower and more dispersed than that in the feed material (Fig. 8(e)), signifying a decrease in total dislocation content. Grain refinement, networking of small equiaxed grains, and decrease in dislocation density all suggest discontinuous dynamic recrystallization (DDRX) as a primary mechanism for microstructure evolution in Cu. Unlike CDRX identified in Al-Mg-Si, which progresses uniformly with an increase in the accumulated strain, DDRX occurs heterogeneously and cyclically. Additionally, the appearance of large grains with no or little local misorientation in Fig. 8(h) is evidence of static (or metadynamic) recrystallization during cooling of AFSD, wherein the local misorientations and dislocations in the larger recrystallized grains are removed due to the migration of HABs. Moreover, given the moderate SFE of Cu [58], dynamic recovery can be a competing process to DDRX under the thermomechanical conditions defined by AFSD. The convolution of all these phenomena forms the final microstructures, in which DDRX and post-dynamic recrystallization particularly lead to the heterogeneous grain and dislocation structures.

Cu-Low and Cu-Mixed both show grain size reduction from the feed material, whereas Cu-High shows an increase in the average grain size. This suggests that deformation and DDRX are more profound in Cu-Low

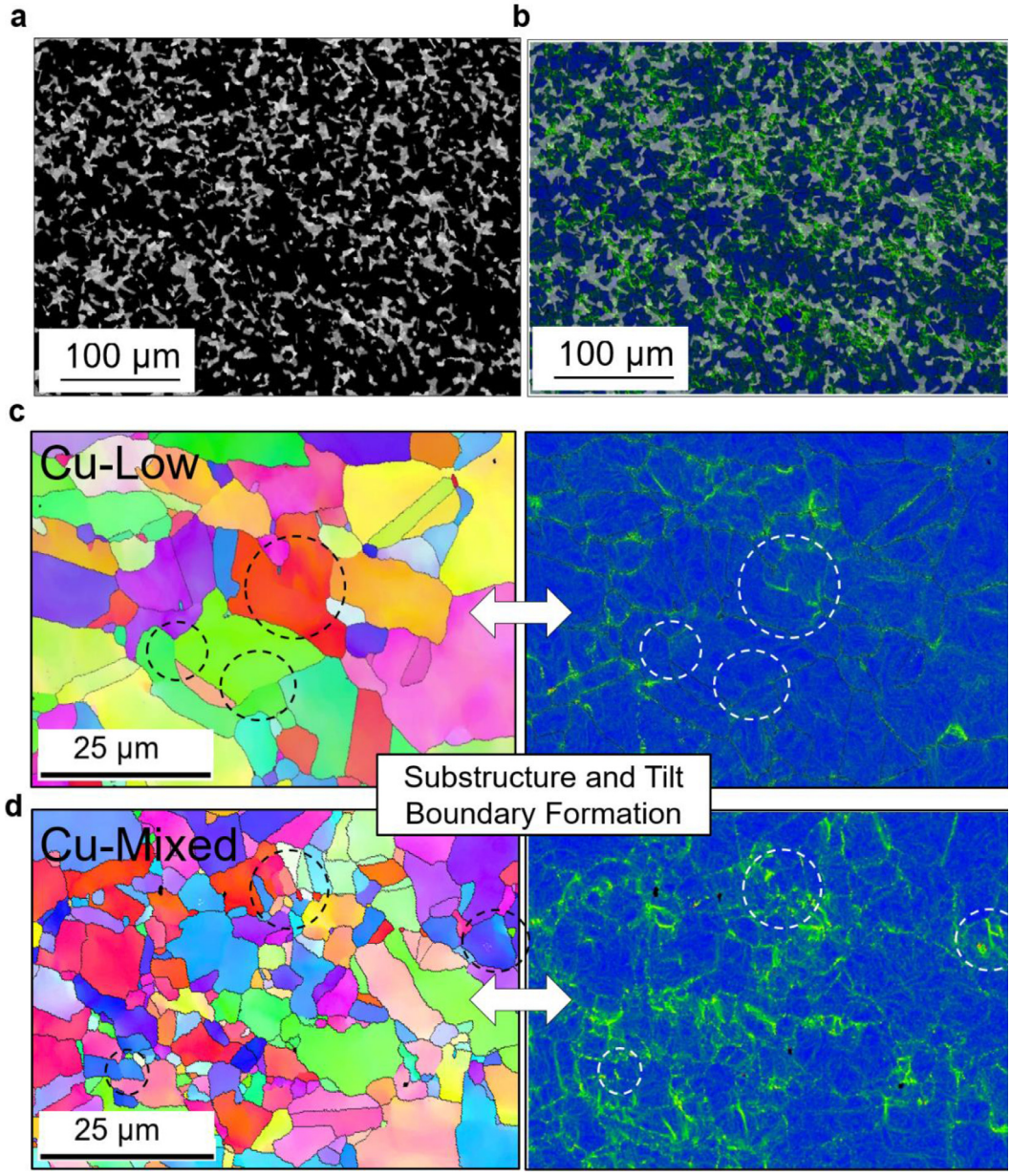

Fig. 13. Restoration mechanisms in AFSD of Cu. (a) Highlight of the grains with the size smaller than the mean grain size. (b) The highlighted small grains overlaid with the KAM map. (c) IPF and (d) KAM maps showing direct evidence for recovery in the Cu deposited at 300 RPM and 1 mm/s. (e) IPF and (f) KAM maps showing the results for Cu deposited at 600 RPM and 1 mm/s. Highlights are areas with apparent substructure forming through the reordering of dislocations within the grains.

and Cu-Mixed than Cu-High. In Section 4.1, we describe how the total strain in Al-Mg-Si is expected to increase with Ω/V in the deposition zone. This conclusion assumes that substantial material flow occurs in the deposition zone and the strain rate depends on the rotation rate Ω. Note that this assumption is not valid for Cu because the deposited material does not rotate in the deposition zone (recall Section 3.1). With the tool rotation primarily applying frictional heating rather than imparting deformation, the shear strain rate in the deposition zone should have a weak dependence on Ω in Cu. The total strain is thus more dependent on the amount of time for deformation through tool-material interactions, which scales with $1/V$. The tool traveling velocity in Cu-High is three times of that in Cu-Low and Cu-Mixed, so the deformation level in Cu-High is expected to be much lower than Cu-Low and Cu-Mixed.

With a lower deformation level, the microstructure evolution in Cu-High is more controlled by post-dynamic recrystallization and the consequential HAB migration in the absence of deformation. As a result, Cu-High contains the least local misorientations and highest fraction of twin boundaries, forming its unique microstructure that is characterized by the large 'clean' grains seen in Figs. 6 and 8. The decreased dislocation density also explains the lowest hardness found in Cu-High (recall Fig. 4).

4.2.2. *Cu-Low vs. Cu-Mixed*

The refined heterogeneous microstructures seen in Cu-Low and Cu-Mixed match well with the previous work on FSW of Cu [59], which is mainly attributed to DDRX. Contrary to this attribution, there is substantial evidence of recovery-induced microstructure evolution that forms substructures and tilt boundaries in both Cu-Low and Cu-Mixed, as shown in Fig. 13(c)–(f). DDRX is expected to primarily result in HAB formation, whereas recovery forms subgrain boundaries and LABs. Cu-

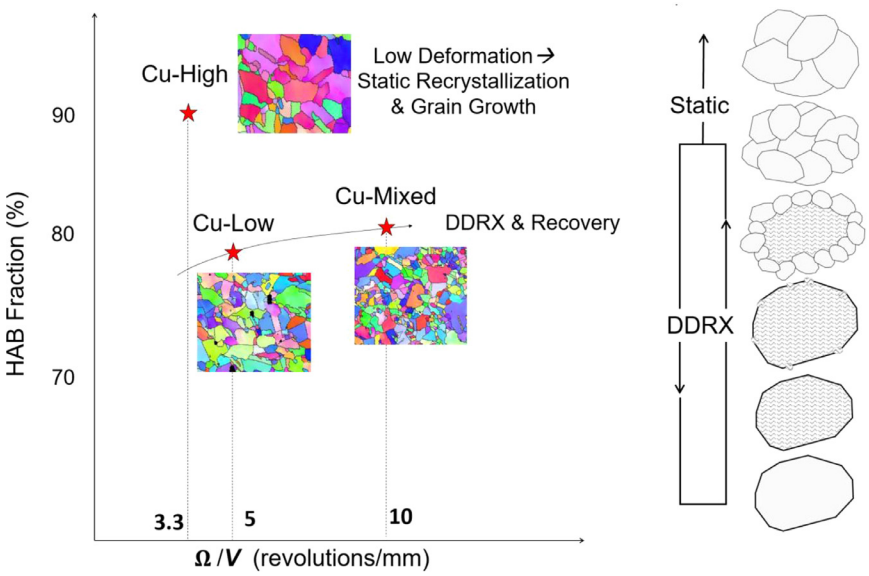

Fig. 14. Processing influences on the microstructure evolution during AFSD of Cu. Left: the HAB fraction, or the degree of recrystallization, is plotted against the characteristic processing parameter Ω/V. Right: illustration of the microstructure evolution process, which is characterized by DDRX during deposition and static recrystallization during cooling.

Low has a higher fraction of LABs, 21.8%, than Cu-Mixed, which has 15.6% LAB. Overall, these findings imply that the final microstructure in Cu-Low and Cu-Mixed is the product of both DDRX and recovery, and recovery plays a more important role in Cu-Low.

Considering the physical processes in AFSD, with the same traveling velocity V, the strain development in Cu-Low and Cu-Mixed should be comparable to each other in the deposition zone—the material is almost stationary without rotation. However, in the transition zone, the material does rotate under the rotating feed-rod inside the hollow channel, rendering Cu-Mixed a higher strain rate and a larger strain than Cu-Low .The peak temperature of Cu-Mixed (992 K) is also higher than Cu-Low (863 K), increasing the effective annealing temperature. The resulting microstructure of Cu-Mixed suggests that the culmination of these effects, i.e., higher strain and higher strain rate in the transition zone along with a higher peak temperature, results in an increased driving force for discontinuous recrystallization, which outcompetes any increase of the recovery rate.

To summarize, owing to the influences of $1/V$, the static recrystallization and grain growth have a particular impact on the final microstructure of Cu-High as compared to Cu-Low and Cu-Mixed. For the latter two, changing Ω can tune the relative contribution of recovery and recrystallization. This phenomenon is illustrated in Fig. 14, which is the Cu counterpart of Fig. 12.

4.3. Comparison of the microstructure evolution between Al-Mg-Si and Cu

One conspicuous difference between AFSD of Al-Mg-Si and Cu lies in the microstructure evolution mechanisms. Al-Mg-Si shows continuous types of microstructure evolution (e.g., dynamic recovery and GDRX), whereas Cu shows discontinuous recrystallization. The different recovery capability of the two materials is the primary reason for such a difference [33]. In Al-Mg-Si, the high SFE leads to the dominance of dynamic recovery over DDRX during deposition, ultimately rendering GDRX the primary microstructure evolution mechanism. In Cu, the moderate SFE causes competition between recovery and discontinuous recrystallization. It is important to note that Cu starts in a pre-deformed (cold-worked) state, which has consequences on the recrystallization behavior: the recrystallization occurs more readily in pre-deformed Cu than in an annealed Cu feed-rod, potentially shifting the balance between recrystallization and recovery. This observation provides another avenue for microstructure manipulation during AFSD, which utilizes pre-treatments of feed material to control the restoration phenomena.

As discussed in Section 3.1, the strain generation during AFSD also appears to be fundamentally different between the two material systems. Substantial material rotation in the deposition zone is observed in Al-Mg-Si but not in Cu, so more strain is generated in the former. Also, the larger transition zone boundary seen in Al-Mg-Si (Fig. 3(c)) inherently imparts more deformation than Cu due to the higher surface area and higher friction coefficient between Al-Al than Cu-Cu [39, 60].

The combined effects of recrystallization mechanisms and deformation levels lead to differences in texture types and magnitudes. Cu has less deformation and more HAB migration due to substantial discontinuous recrystallization. As a result, it has a much weaker deformation texture than in Al-Mg-Si. Comparing the orientation of the formed shear textures, the Cu samples are all nearly identical, but the Al-Mg-Si deposits vary in orientation. This suggests that the deformation gradient applied by AFSD varies little with process variables for Cu, but greatly for Al-Mg-Si. It is also expected that the evolution history of deformation texture is fundamentally different between Cu and Al-Mg-Si: the texture in Cu may form mainly in the transition zone, whereas the texture in Al-Mg-Si develops in both the transition zone and deposition zone.

5. Conclusions

We have investigated the microstructure evolution and its dependence on process variables in AFSD-based solid-state metal additive manufacturing. In both Al-Mg-Si and Cu, the resultant grain structure, local misorientation, and texture are sensitively dependent on the process variables, such as tool head rotation rate Ω and traveling velocity V. This renders a large microstructure design space based around the progress of recrystallization through process control. Distinct microstructural features are found between Al-Mg-Si and Cu, owing to their different microstructure evolution mechanisms and strain generation processes. The most important conclusions include:

- AFSD results in a relatively homogeneous microstructure in Al-Mg-Si with extensive subgrain formation. The microstructure refinement mechanism is mainly GDRX, which is characterized by severe grain elongation and pinch-off of grain boundary serrations.
- AFSD results in a heterogeneous grain structure in Cu, and there are more local misorientations in smaller grains. This is caused by DDRX during deposition as well as static restoration during cooling.
- For Al-Mg-Si, the substantial material rotation in the deposition zone gives rise to the correlation between Ω/V and the strain level, which nominally increases the degree of recrystallization. Meanwhile, the

peak temperature influences the precipitates in the feed material and therefore the recrystallization rate.

- For Cu, the strain level is more dependent on the tool-material interaction time and therefore the tool traveling velocity V. When V is sufficiently large and the strain level is low, the microstructure evolution is dominated by post-dynamic recrystallization and the consequential HAB migration.
- The distinct recrystallization types (due to different SFE levels) and strain generation processes between Al-Mg-Si and Cu result in stronger crystallographic textures in the former than the latter.

These findings provide valuable strategies for controlling the microstructures formed by AFSD. For example, the SFE of a material can be adjusted via solute atoms [61, 62] so that the restoration modes can be tuned accordingly. Adding second-phase particles can have a dramatic effect on microstructure evolution rates, allowing for similar degrees of recrystallization at different strain levels. Moreover, by changing the tool material or tool coating, one could change the friction coefficient at the tool-material interface to adjust the strain generation process.

Declaration of Competing Interest

The authors declare that they have no known competing financial interests or personal relationships that could have appeared to influence the work reported in this paper.

Acknowledgement

H. Z. Yu would like to acknowledge the support from National Science Foundation (CMMI-1853893). The authors would also like to thank Dylan Petersen for helpful comments. This work was performed in part at the Nanoscale Characterization and Fabrication Laboratory, which is supported by the Virginia Tech National Center for Earth and Environmental Nanotechnology Infrastructure (NanoEarth)—a member of the National Nanotechnology Coordinated Infrastructure (NNCI), supported by NSF (ECCS 1542100 and ECCS 2025151).

References

[1] N. Tuncer, A. Bose, Solid-state metal additive manufacturing: a review, JOM 72 (2020) 3090–3111.
[2] S. Yin, P. Cavaliere, B. Aldwell, R. Jenkins, H. Liao, W. Li, R. Lupoi, Cold spray additive manufacturing and repair: fundamentals and applications, Addit. Manuf. 21 (2018) 628–650.
[3] R.J. Friel, R.A. Harris, Ultrasonic additive manufacturing – a hybrid production process for novel functional products, Proc. CIRP 6 (2013) 35–40.
[4] F. Khodabakhshi, A.P. Gerlich, Potentials and strategies of solid-state additive friction-stir manufacturing technology: a critical review, J. Manuf. Process. 36 (2018) 77–92.
[5] H.Z. Yu, M.E. Jones, G.W. Brady, R.J. Griffiths, D. Garcia, H.A. Rauch, C.D. Cox, N. Hardwick, Non-beam-based metal additive manufacturing enabled by additive friction stir deposition, Scr. Mater. 153 (2018) 122–130.
[6] I. Zein, D.W. Hutmacher, K.C. Tan, S.H. Teoh, Fused deposition modeling of novel scaffold architectures for tissue engineering applications, Biomaterials 23 (4) (2002) 1169–1185.
[7] S.H. Ahn, M. Montero, D. Odell, S. Roundy, K. Wright Paul, Anisotropic material properties of fused deposition modeling ABS, Rapid Prototyp. J. 8 (4) (2002) 248–257.
[8] M.E.J. Perry, R.J. Griffiths, D. Garcia, J.M. Sietins, Y. Zhu, H.Z. Yu, Morphological and microstructural investigation of the non-planar interface formed in solid-state metal additive manufacturing by additive friction stir deposition, Addit. Manuf. 35 (2020) 101293.
[9] D. Garcia, W.D. Hartley, H.A. Rauch, R.J. Griffiths, R. Wang, Z.J. Kong, Y. Zhu, H.Z. Yu, In situ investigation into temperature evolution and heat generation during additive friction stir deposition: a comparative study of Cu and Al-Mg-Si, Addit. Manuf. 34 (2020) 101386.
[10] R.J. Griffiths, M.E.J. Perry, J.M. Sietins, Y. Zhu, N. Hardwick, C.D. Cox, H.A. Rauch, H.Z. Yu, A perspective on solid-state additive manufacturing of aluminum matrix composites using MELD, J. Mater. Eng. Perform. 28 (2) (2019) 648–656.
[11] D. Garcia, M.E. Jones, Y. Zhu, H.Z. Yu, Mesoscale design of heterogeneous material systems in multi-material additive manufacturing, J. Mater. Res. 33 (1) (2018) 58–67.
[12] H.Z. Yu, S.R. Cross, C.A. Schuh, Mesostructure optimization in multi-material additive manufacturing: a theoretical perspective, J. Mater. Sci. 52 (8) (2017) 4288–4298.
[13] R.S. Mishra, Z.Y. Ma, Friction stir welding and processing, Mater. Sci. Eng. R Rep. 50 (1) (2005) 1–78.
[14] A. Arora, Z. Zhang, A. De, T. DebRoy, Strains and strain rates during friction stir welding, Scr. Mater. 61 (9) (2009) 863–866.
[15] R. Kumar, V. Pancholi, R.P. Bharti, Material flow visualization and determination of strain rate during friction stir welding, J. Mater. Process. Technol. 255 (2018) 470–476.
[16] F.J. Humphreys, M. Hatherly, Recrystallization and related annealing phenomena in: F.J. Humphreys, M. Hatherly (Eds.), Elsevier, Oxford, 2004, pp. 67–89.
[17] T. Sakai, A. Belyakov, R. Kaibyshev, H. Miura, J.J. Jonas, Dynamic and post-dynamic recrystallization under hot, cold and severe plastic deformation conditions, Prog. Mater. Sci. 60 (2014) 130–207.
[18] Y.S. Sato, M. Urata, H. Kokawa, K. Ikeda, Hall–Petch relationship in friction stir welds of equal channel angular-pressed aluminium alloys, Mater. Sci. Eng. A 354 (1) (2003) 298–305.
[19] M.D. Sangid, H.J. Maier, H. Sehitoglu, The role of grain boundaries on fatigue crack initiation – an energy approach, Int. J. Plast. 27 (5) (2011) 801–821.
[20] S. Bechtle, M. Kumar, B.P. Somerday, M.E. Launey, R.O. Ritchie, Grain-boundary engineering markedly reduces susceptibility to intergranular hydrogen embrittlement in metallic materials, Acta Mater. 57 (14) (2009) 4148–4157.
[21] R.W. Fonda, J.F. Bingert, K.J. Colligan, Development of grain structure during friction stir welding, Scr. Mater. 51 (3) (2004) 243–248.
[22] P.B. Prangnell, C.P. Heason, Grain structure formation during friction stir welding observed by the 'stop action technique', Acta Mater. 53 (11) (2005) 3179–3192.
[23] U.F.H.R. Suhuddin, S. Mironov, Y.S. Sato, H. Kokawa, Grain structure and texture evolution during friction stir welding of thin 6016 aluminum alloy sheets, Mater. Sci. Eng. A 527 (7) (2010) 1962–1969.
[24] O.G. Rivera, P.G. Allison, L.N. Brewer, O.L. Rodriguez, J.B. Jordon, T. Liu, W.R. Whittington, R.L. Martens, Z. McClelland, C.J.T. Mason, L. Garcia, J.Q. Su, N. Hardwick, Influence of texture and grain refinement on the mechanical behavior of AA2219 fabricated by high shear solid state material deposition, Mater. Sci. Eng. A 724 (2018) 547–558.
[25] O.G. Rivera, P.G. Allison, J.B. Jordon, O.L. Rodriguez, L.N. Brewer, Z. McClelland, W.R. Whittington, D. Francis, J. Su, R.L. Martens, N. Hardwick, Microstructures and mechanical behavior of Inconel 625 fabricated by solid-state additive manufacturing, Mater. Sci. Eng. A 694 (2017) 1–9.
[26] R.J. Griffiths, D.T. Petersen, D. Garcia, H.Z. Yu, Additive friction stir-enabled solid-state additive manufacturing for the repair of 7075 aluminum alloy, Appl. Sci. 9 (17) (2019).
[27] D.Z. Avery, B.J. Phillips, C.J.T. Mason, M. Palermo, M.B. Williams, C. Cleek, O.L. Rodriguez, P.G. Allison, J.B. Jordon, Influence of grain refinement and microstructure on fatigue behavior for solid-state additively manufactured Al-Zn-Mg-Cu alloy, Metall. Mater. Trans. A 51 (6) (2020) 2778–2795.
[28] C. Körner, Additive manufacturing of metallic components by selective electron beam melting — a review, Int. Mater. Rev. 61 (5) (2016) 361–377.
[29] J.H. Martin, B.D. Yahata, J.M. Hundley, J.A. Mayer, T.A. Schaedler, T.M. Pollock, 3D printing of high-strength aluminium alloys, Nature 549 (7672) (2017) 365–369.
[30] B.A.A. Rutherford, D. Z., B.J. Phillips, H.M. Rao, K.J. Doherty, P.G. Allison, L.N. Brewer, J.B. Jordon, Effect of thermomechanical processing on fatigue behavior in solid-state additive manufacturing of Al-Mg-Si alloy, Met. (Basel) 10 (2020) 947.
[31] M.P. Muzyk, Z., K.J. Kurzydłowski, Generalized stacking fault energies of aluminum alloys–density functional theory calculations, Met. (Basel) 8 (2018) 823.
[32] Y.H. Zhao, X.Z. Liao, Y.T. Zhu, Z. Horita, T.G. Langdon, Influence of stacking fault energy on nanostructure formation under high pressure torsion, Mater. Sci. Eng. A 410-411 (2005) 188–193.
[33] A. Heidarzadeh, T. Saeid, V. Klemm, A. Chabok, Y. Pei, Effect of stacking fault energy on the restoration mechanisms and mechanical properties of friction stir welded copper alloys, Mater. Des. 162 (2019) 185–197.
[34] D. Hull, D.J. Bacon, in: Introduction to Dislocations, Materials Science and Technology (New York, N Y), 37, Butterworth-Heinemann, Oxford, 2011, p. 1. vonline resource.
[35] Engineering ToolBox, Modulus of Rigidity., [online] Available at: https://www.engineeringtoolbox.com/modulus-rigidity-d_946.html (2005).
[36] Engineering ToolBox, Young's modulus - tensile and yield strength for common materials., [online] Available at: https://www.engineeringtoolbox.com/young-modulus-d_417.html (2003).
[37] H. Schmidt, J. Hattel, J. Wert, An analytical model for the heat generation in friction stir welding, Model. Simul. Mater. Sci. Eng. 12 (1) (2003) 143–157.
[38] J. Schneider, R. Beshears, A.C. Nunes, Interfacial sticking and slipping in the friction stir welding process, Mater. Sci. Eng. A 435-436 (2006) 297–304.
[39] W.G. Beare, F.P. Bowden, T.M. Lowry, Physical properties of surfaces I - Kinetic friction, Philos. Trans. R. Soc. Lond. Ser. A Math. Phys. Sci. 234 (741) (1935) 329–354.
[40] A. Simar, Y. Bréchet, B. de Meester, A. Denquin, C. Gallais, T. Pardoen, Integrated modeling of friction stir welding of 6xxx series Al alloys: process, microstructure and properties, Prog. Mater. Sci. 57 (1) (2012) 95–183.
[41] B.J. Phillips, D.Z. Avery, T. Liu, O.L. Rodriguez, C.J.T. Mason, J.B. Jordon, L.N. Brewer, P.G. Allison, Microstructure-deformation relationship of additive friction stir-deposition Al–Mg–Si, Materialia 7 (2019) 100387.
[42] X.C. Liu, Y.F. Sun, T. Nagira, K. Ushioda, H. Fujii, Evaluation of dynamic development of grain structure during friction stir welding of pure copper using a quasi in situ method, J. Mater. Sci. Technol. 35 (7) (2019) 1412–1421.
[43] N. Xu, R. Ueji, H. Fujii, Dynamic and static change of grain size and texture of copper during friction stir welding, J. Mater. Process. Technol. 232 (2016) 90–99.
[44] R.W. Fonda, K.E. Knipling, Texture development in friction stir welds, Sci. Technol. Weld. Join. 16 (4) (2011) 288–294.

[45] F. Montheillet, M. Cohen, J.J. Jonas, Axial stresses and texture development during the torsion testing of Al, Cu and α-Fe, Acta Metall. 32 (11) (1984) 2077–2089.
[46] W. Cai, J. Mabon, P. Bellon, Crystallographic textures and texture transitions induced by sliding wear in bronze and nickel, Wear 267 (1) (2009) 485–494.
[47] L.S. Tóth, K.W. Neale, J.J. Jonas, Stress response and persistence characteristics of the ideal orientations of shear textures, Acta Metall. 37 (8) (1989) 2197–2210.
[48] R.W. Fonda, K.E. Knipling, J.F. Bingert, Microstructural evolution ahead of the tool in aluminum friction stir welds, Scr. Mater. 58 (5) (2008) 343–348.
[49] G.R. Canova, U.F. Kocks, J.J. Jonas, Theory of torsion texture development, Acta Metall. 32 (2) (1984) 211–226.
[50] X.C. Liu, Y.F. Sun, H. Fujii, Clarification of microstructure evolution of aluminum during friction stir welding using liquid CO_2 rapid cooling, Mater. Des. 129 (2017) 151–163.
[51] J.-.Q. Su, T.W. Nelson, C.J. Sterling, Microstructure evolution during FSW/FSP of high strength aluminum alloys, Mater. Sci. Eng. A 405 (1) (2005) 277–286.
[52] K.V. Jata, S.L. Semiatin, Continuous dynamic recrystallization during friction stir welding of high strength aluminum alloys, Scr. Mater. 43 (8) (2000) 743–749.
[53] T.R. McNelley, S. Swaminathan, J.Q. Su, Recrystallization mechanisms during friction stir welding/processing of aluminum alloys, Scr. Mater. 58 (5) (2008) 349–354.
[54] A.P. Reynolds, Flow visualization and simulation in FSW, Scr. Mater. 58 (5) (2008) 338–342.
[55] J.R. DavisJ.R.D. Associates, A.S.M.I.H. Committee, Aluminum and Aluminum Alloys, ASM International, 1993.
[56] C. Gallais, A. Denquin, Y. Bréchet, G. Lapasset, Precipitation microstructures in an AA6056 aluminium alloy after friction stir welding: characterisation and modelling, Mater. Sci. Eng. A 496 (1) (2008) 77–89.
[57] K. Huang, K. Marthinsen, Q. Zhao, R.E. Logé, The double-edge effect of second-phase particles on the recrystallization behaviour and associated mechanical properties of metallic materials, Prog. Mater. Sci. 92 (2018) 284–359.
[58] J.R. DavisA.S.M.I.H. Committee, ASM Specialty Handbook - Copper and Copper Alloys, ASM International, 2001.
[59] S. Mironov, K. Inagaki, Y.S. Sato, H. Kokawa, Microstructural evolution of pure copper during friction-stir welding, Philos. Mag. 95 (4) (2015) 367–381.
[60] Friction and Friction Coefficients., Engineering ToolBox [online] Available (https://www.engineeringtoolbox.com/friction-coefficients-d_778.html) (2004).
[61] L.H. Liu, J.H. Chen, T.W. Fan, Z.R. Liu, Y. Zhang, D.W. Yuan, The possibilities to lower the stacking fault energies of aluminum materials investigated by first-principles energy calculations, Comput. Mater. Sci. 108 (2015) 136–146.
[62] Q.Q. Shao, L.H. Liu, T.W. Fan, D.W. Yuan, J.H. Chen, Effects of solute concentration on the stacking fault energy in copper alloys at finite temperatures, J. Alloys Compd. 726 (2017) 601–607.